Weierstraß-Institut
für Angewandte Analysis und Stochastik
Leibniz-Institut im Forschungsverbund Berlin e. V.

Preprint ISSN 0946 – 8633

Modeling and simulations of beam stabilization in edge-emitting broad area semiconductor devices

Mindaugas Radziunas[1], Raimondas Čiegis[2]

submitted: June 24, 2013

[1] Weierstrass Institute
Mohrenstrasse 39
10117 Berlin, Germany
E-Mail: Mindaugas.Radziunas@wias-berlin.de

[2] Vilnius Gediminas Technical University
Saulėtekio al. 11
LT-10223 Vilnius, Lithuania
E-Mail: rc@vgtu.lt

No. 1806
Berlin 2013

2010 *Mathematics Subject Classification.* 65M06, 65M20, 65M99, 35Q60, 65M12.

Key words and phrases. Broad area device, traveling wave model, numerical scheme, simulations, beam improvement .

The work of M. R. was supported by DFG Research Center MATHEON “Mathematics for key technologies: Modelling, simulation, and optimization of real-world processes”.

Edited by
Weierstraß-Institut für Angewandte Analysis und Stochastik (WIAS)
Leibniz-Institut im Forschungsverbund Berlin e. V.
Mohrenstraße 39
10117 Berlin
Germany

Fax: +49 30 20372-303
E-Mail: `preprint@wias-berlin.de`
World Wide Web: `http://www.wias-berlin.de/`

Abstract

A 2+1 dimensional PDE traveling wave model describing spatial-lateral dynamics of edge-emitting broad area semiconductor devices is considered. A numerical scheme based on a split-step Fourier method is presented and implemented on a parallel compute cluster. Simulations of the model equations are used for optimizing of existing devices with respect to the emitted beam quality, as well as for creating and testing of novel device design concepts.

1 Introduction

High power high brightness edge-emitting (EE) broad area semiconductor (BAS) lasers and optical amplifiers are compact devices playing a key role in different laser technologies. They have a relatively simple geometry (Fig. 1(a)) allowing an efficient pumping through a broad electric contact on the top of the device and are able to operate at the high power (tens of Watts) regimes. However, once operated at high power regimes, BAS devices suffer from a relatively low quality of the emitted beam which has undesirable broad optical and lateral spectra. A high quality of the beam amplified in BAS amplifiers or generated by BAS lasers is a very important issue of the modern semiconductor laser technology, and there are several BAS device concepts for improving of the emitted beam.

Mathematical modeling, simulations and analysis play a significant role in optimization of existing devices or creation of novel design concepts [1]. Typically, the length (z dimension) and width (x-dimension) of EE BAS devices (see Fig. 1(a)) are in a few millimeter and hundreds of micrometer range, respectively, whereas the height (y dimension) of the active zone where the optical beam is generated and amplified is, typically, not larger than a micrometer. Since full 3-dimensional dynamical simulations of semiconductor devices with different spatial and temporal scales is not possible, we replace all y-dependent quantities by some effective vertical averages. To simulate the generation and/or propagation of the optical fields along the cavity of EE BAS devices we use a 2+1 dimensional system of PDEs, described briefly in this paper. The model is based on the traveling wave (TW) equations for counter-propagating and laterally diffracted slowly varying optical fields which are coupled to the ODE for induced polarizations and diffusive rate equation for carrier densities [2, 3]. The well-posedness of this model was studied in [4], while different algorithms used for the numerical integration of the model were considered in [5, 6, 7].

Precise dynamic simulations of long and broad or tapered devices and tuning/optimization of the model with respect to one or several parameters, require huge CPU time and memory resources. A proper resolution of rapidly oscillating fields in typical BAS devices on a sufficiently large optical frequency range requires a fine space ($10^6 - 10^7$ mesh points) and time (up to 10^6 points for typical 5 ns transients) discretization. Dynamic simulations of such devices can easily take one or even several days of computations on a single processor computer. Some speedup of computations can be achieved by using problem-dependent relations of the

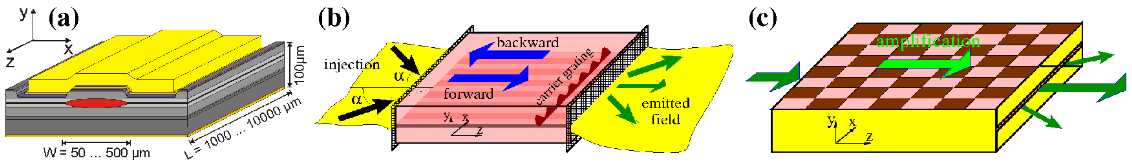

Figure 1: Schemes of different EE BAS device configurations. (a): standard EE BAS laser. (b): BAS laser with a dual angular plane wave injection. (c): BAS amplifier with a spatially periodic electrical contact.

grid steps, including also variable steps in the lateral dimension. All these grid optimizations, however, are not sufficient when one- or a few- parameter studies with the simulation times up to 1000 ns should be performed. It is obvious, that the required computations in an acceptable time can only be done by means of parallel computers and parallel solvers.

In this paper we present a split-step Fourier method based numerical algorithm for the integration of the 2+1 dimensional traveling wave model of BAS devices. It was implemented on the parallel compute cluster at the Weierstrass Institute in Berlin and was successfully used for simulations of different BAS devices with an improved quality of the beam [3, 8, 9, 10, 11]. In this paper we present two examples of such BAS devices (see Fig. 1(b) and (c) which were proposed in our theoretical papers [12, 13, 14]. In the first device, a pair of coherently injected plane waves at the adjoint angles to the laser axis (Fig. 1(b)) can create a periodic carrier grating, which in turn can suppress all but one lateral modes of the laser [12, 13]. The second device has periodically modulated (PM) electrical contact or active zone in both spatial directions (Fig. 1(c)), what can lead to a significant improvement of the amplified beam in BAS amplifiers [14].

2 Mathematical model

After an appropriate scaling, the traveling wave (TW) model for longitudinal-lateral dynamics of the complex slowly varying amplitudes of the counter-propagating fields $E^{\pm}(z,x,t)$, polarization functions $P^{\pm}(z,x,t)$ and real carrier density function $N(z,t,x)$ can be written as follows [7]:

$$\begin{aligned}
&\left(\tfrac{\partial}{\partial t} \pm \tfrac{\partial}{\partial z}\right) E^{\pm} = -\tfrac{i}{2}\tfrac{\partial^2}{\partial x^2} E^{\pm} - i\left[\beta(N,\|E\|^2) - i\tfrac{\mathcal{D}}{2}\right] E^{\pm} - i\kappa^{\mp} E^{\mp},\\
&\tfrac{\partial}{\partial t} P^{\pm} = i\overline{\omega} P^{\pm} + \overline{\gamma}\left(E^{\pm} - P^{\pm}\right),\\
&\tfrac{1}{\mu}\tfrac{\partial}{\partial t} N = D\tfrac{\partial^2}{\partial x^2} N + I(z,x) - R(N) - \Re e \sum_{\nu=\pm} E^{\nu *}\left[G(N,|E^{\pm}|^2) - \mathcal{D}\right] E^{\nu},
\end{aligned} \tag{1}$$

where $\|E\|^2 = |E^+|^2 + |E^-|^2$ is proportional to the local field intensity, whereas the operators β, $\mathcal{D}$ and functions G, $\tilde{n}$, R denote the propagation factor, the Lorentzian approximation of the material gain dispersion, the gain peak value, the refractive index change, and the spontaneous recombination, respectively:

$$\begin{aligned}
&\beta(N,|E^{\pm}|^2) = \Delta - \tilde{n}(N) + \tfrac{i\left(G(N,\|E\|^2)-\alpha\right)}{2}, \quad \mathcal{D}E^{\pm}{=}\overline{g}\,(E^{\pm}-P^{\pm})\,,\\
&G(N,\|E\|^2) = \tfrac{g' N_{tr}}{1+\varepsilon\|E\|^2}\log\left(\tfrac{\max(N,N_*)}{N_{tr}}\right), \quad \tilde{n}(N) = 2\sigma N_{tr}\sqrt{N/N_{tr}},\\
&R(N) = AN + BN^2 + CN^3.
\end{aligned} \tag{2}$$

In general, this model should be considered in the unbounded region $Q = Q_{z,x} \times (0,T]$, where $Q_{z,x} = \{(z,x):\ (z,x) \in (0,L) \times \mathbf{R}\}$ is the spatial domain, L represents the device length, x is the coordinate of the unbounded lateral axis of the device, and T is the length of the time interval where we perform the integration. In our numerical simulations we choose a large enough lateral interval $[-X,X]$ containing the considered BAS device and assume that the field and carrier density functions $E^{\pm}$ and N are periodic along the lateral axis:

$$E^{\pm}(z,x+2X,t) = E^{\pm}(z,x,t), \;\; N(z,x+2X,t) = N(z,x,t), \;\; (z,x,t) \in Q. \tag{3}$$

This assumption restricts our considerations of the model equations to the truncated domain $Q^X = Q^X_{z,x} \times (0,T]$, $Q^X_{z,x} = \{(z,x):\ (z,x) \in (0,L) \times [-X,X]\}$. The boundary conditions for the optical fields $E^{\pm}$ at the device facets $(z,x) \in 0 \times [-X,X]$ and $(z,x) \in L \times [-X,X]$ in (1) are given by

$$\begin{aligned}
&E^{-}(L,x,t) = r_1(x)\,E^{+}(L,x,t) + F\left[E^{+}(L,\cdot,t-\tau)\right],\\
&E^{+}(0,x,t) = r_0(x)\,E^{-}(0,x,t) + a(x,t), \qquad (x,t) \in [-X,X] \times [0,T],
\end{aligned} \tag{4}$$

where $r_{0,1}$, a and F are the field amplitude reflectivity coefficients, the complex amplitude of the optical field injection, and another optical source determined by the reinjected delayed optical field [10], respectively. The initial conditions

$$E^{\pm}(z,x,0) = E^{\pm}_0(z,x), \;\; P^{\pm}(z,x,0) = P^{\pm}_0(z,x), \;\; N(z,x,0) = N_0(z,x), \tag{5}$$

are defined for $(z,x) \in Q^X_{z,x}$. If properly stated, they are not important, since after some transients the trajectories approach one of the stable attractors.

The coefficients $\kappa^{\pm}$, Δ, α, g', σ, N_{tr}, N_*, ε, μ, D, I, A, B and C represent the complex field coupling due to the Bragg grating, the static detuning due to the built-in refractive index profile, the internal losses of the field, the differential gain, the differential index, the carrier density at the transparency, the gain clamping carrier density, the nonlinear gain compression, the scaling factor related to the ratio of the photon and carrier life times, the carrier diffusion coefficient, the current injection density, and three recombination factors, respectively. Finally, $\overline{g}$, $\overline{\omega}$ and $\overline{\gamma}$ denote the amplitude, the central frequency and the half width at half maximum of the Lorentzian fitting of the gain profile.

Most of the parameters are spatially non-homogeneous and even discontinuous depending on the device geometry. More details about the meaning and typical values of all parameters can be found in [2, 3]. Normalization of the equations and typical values of the normalized parameters are given in [7]. It is noteworthy, that $\overline{\gamma} \approx 10^2 - 10^3$ and $\mu \approx 10^{-3}$ represent the fast relaxation of the polarizations $P^{\pm}$ and slow dynamics of the carrier density N, respectively. Typical size of the dimensionless domain is determined by $X \approx 5 - 30$ and $L \approx 1 - 10$, whereas $D \approx 0.5$ and most of other parameters are of order $\mathcal{O}(1)$.

3 Numerical scheme

The computation domain Q^X is discretized using a uniform in space and time grid $Q_h^X = Q_{h,z,x}^X \times \omega_{h,t}$, where $Q_{h,z,x}^X = \omega_{h,z} \times \omega_{h,x}$, and

$$\begin{aligned} \omega_{h,x} &= \{x_j: \;\; x_j = j\,h_x, \;\; j = -J/2, \dots, J/2-1, \; h_x = 2X/J\}, \\ \omega_{h,z} &= \{z_k: \;\; z_k = k\,h, \;\; k = 0, \dots, K, \; h = L/K\}, \\ \omega_{h,t} &= \{t_m: \;\; t_m = m\,h, \;\; m = 0, \dots, M, \; M = T/h\}. \end{aligned}$$

The time discretization step h is equal to the spatial step in z-direction, what allows an accurate optical field propagation along the characteristic lines $z \pm t = \mathrm{const}$. We note, that h is the maximal allowed time step: its further increasing violates the Courant-Friedrichs-Lewy CFL) condition and, therefore, stability of the numerical schemes.

All spatially depending parameters $P(z,x)$, spatially and temporarily depending functions $F(x,t)$ and unknown functions $U(z,x,t)$ in Eqs. (1)-(5) are approximated by their grid analogs defined on Q_h^X:

$$P_{k,j} = P(z_k, x_j), \quad F_j^m = F(x_j, t), \quad U_{k,j}^m \approx U(z_k, x_j, t_m).$$

When constructing numerical schemes we exploit a discrete Fourier transform of complex and real laterally-periodic functions $U(z,x,t)$, where $U = E^\pm$ or $U = N$. Namely, we assume that a complex function $U_j(z,t) := U(z, x_j, t)$ (representing the fields E^+ and E^-) on the uniform lateral mesh $\omega_{h,x}$ can be expressed as a linear combination of the orthonormal grid-functions $e^{i\pi\ell x_j/X}|_{\ell=-J/2}^{J/2-1}$:

$$U_j(z,t) = \left[\mathcal{F}^{-1}\left(\widehat{U}_\ell(z,t)\big|_{\ell=-J/2}^{J/2-1}\right)\right]_j := \frac{1}{J}\sum_{\ell=-J/2}^{J/2-1} \widehat{U}_\ell(z,t) e^{i\pi\ell x_j/X}, \tag{6}$$

where the Fourier coefficients $\widehat{U}_\ell(z,t)$ are defined as

$$\widehat{U}_\ell^\pm(z,t) = \left[\mathcal{F}\left(U_j(z,t)\big|_{j=-J/2}^{J/2-1}\right)\right]_\ell := \sum_{j=-J/2}^{J/2-1} U_j(z,t) e^{-i\pi\ell x_j/X}. \tag{7}$$

These transforms are used for the approximation of $\frac{\partial^2}{\partial x^2}U$ at any grid point x_j:

$$\frac{\partial^2}{\partial x^2} U(z, x_j, t) \approx \frac{1}{J}\sum_{\ell=-J/2}^{J/2-1} \left(-\frac{\pi^2\ell^2}{X^2}\right) \widehat{U}_\ell(z,t) e^{i\pi\ell x_j/X}. \tag{8}$$

When U represents the carrier density N and is *real*, it can be expressed as a linear combination of the real orthogonal grid-functions $\cos(\pi\ell x_j/X)|_{\ell=0}^{J/2}$, and $\sin(\pi\ell x_j/X)|_{\ell=1}^{J/2-1}$. An equivalent *complex* expression of such combination can be written as (6) with the *complex* Fourier coefficients (7) satisfying the relations $\widehat{N}_{-J/2} = \widehat{N}_{-J/2}^*$ and $\widehat{N}_\ell = \widehat{N}_{-\ell}^*$, $\ell = 0, \dots, J/2-1$.

3.1 Splitting scheme

The TW model (1)-(5) is integrated numerically using a splitting scheme, where the lateral field diffraction and carrier diffusion are resolved with the fast Fourier transform, and the remaining coupled hyperbolic system in (1) is integrated along the characteristics using finite differences. The stiff ODE for the polarization functions $P^{\pm}$ in (1) ($\overline{\gamma}$ is large !) is resolved using an exponentially weighted scheme with the forward values for $E^{\pm}$, which ensures, that $\lim_{\overline{\gamma}\to\infty} P^{\pm} = E^{\pm}$.

Let us assume, that the grid functions $E^{\pm,m}_{k,j}$, $P^{\pm,m}_{k,j}$ and $N^m_{k,j}$ are known for the time layer t^m. In the time-stepping algorithm we split the diffraction, diffusion processes and the nonlinear interaction. To find the grid functions at the new time layer t^{m+1} we proceed as follows. In the first step of our algorithm we consider only the nonlinear interaction and make a simple prediction of the carrier density at the new time layer:

$$\begin{aligned} \tfrac{\widetilde{N}^{m+1}_{k,j} - N^m_{k,j}}{\mu h} = \; & -\left(G(N^m_{k,j}, \|E^m_{k,j}\|^2) - \overline{g}\right) \|E^m_{k,j}\|^2 - \overline{g}\, \Re e \sum_{\nu=\pm} E^{\nu,m*}_{k,j} P^{\nu,m}_{k,j} \\ & + I_{k,j} - \tfrac{\widetilde{N}^{m+1}_{k,j} R\left(N^m_{k,j}\right)}{N^m_{k,j}}, \qquad k = 0,\dots,K, \quad j = 1,\dots,M. \end{aligned} \tag{9}$$

Due to the slow carrier dynamics (the diffusion is moderate and the factor μ is small) we use a simple implicit-explicit linearized scheme with a totally ignored carrier diffusion at this step.

In the next step we neglect the field diffraction and find intermediate approximations for the optical fields and new polarization functions:

$$\begin{aligned} \tfrac{\widetilde{E}^{\pm,m+1}_{k,j} - E^{\pm,m}_{k\mp1,j}}{h} = & -i \tfrac{\beta\left(\widetilde{N}^{m+1}_{k,j}, \|E^m_{k,j}\|^2\right)\widetilde{E}^{\pm,m+1}_{k,j} + \beta\left(N^m_{k\mp1,j}, \|E^m_{k\mp1,j}\|^2\right) E^{\pm,m}_{k\mp1,j}}{2} \\ & - \tfrac{\overline{g}_{k,j}(\widetilde{E}^{\pm,m+1}_{k,j} - P^{\pm,m+1}_{k,j}) + \overline{g}_{k\mp1,j}(E^{\pm,m}_{k\mp1,j} - P^{\pm,m}_{k\mp1,j})}{4} \\ & - i \tfrac{\kappa^{\mp}_{k,j}\widetilde{E}^{\mp,n+1}_{k,j} + \kappa^{\mp}_{k\mp1,j} E^{\mp,m}_{k\mp1,j}}{2}, \qquad k, k\mp1 \in \{0,\dots,K\}; \\ \widetilde{E}^{+,m+1}_{0,j} = & \; r_{0,j}\widetilde{E}^{-,m+1}_{0,j} + a^{m+1}_j, \quad \widetilde{E}^{-,m+1}_{K,j} = r_{1,j}\widetilde{E}^{+,m+1}_{K,j} + F_h\left[E^{+,m+1-\frac{\tau}{h}}_{K,\cdot}\right], \\ P^{\pm,m+1}_{k,j} = & \; \tfrac{\overline{\gamma}_{k,j}\left(1 - e^{(i\overline{\omega}_{k,j} - \overline{\gamma}_{k,j})h}\right)}{\overline{\gamma}_{k,j} - i\overline{\omega}_{k,j}} \widetilde{E}^{\pm,m+1}_{k,j} + e^{(i\overline{\omega}_{k,j} - \overline{\gamma}_{k,j})h} P^{\pm,m}_{k,j}, \; k = 0,\dots,K, \\ & j = 1,\dots,M. \end{aligned} \tag{10}$$

We note, that the scheme above is linear with respect to $\widetilde{E}^{\pm,m+1}_{k,j}$ and $P^{\pm,m+1}_{k,j}$ and can be separately resolved for each $k = 0,\dots,K$.

In the final step of our algorithm we take into account the carrier diffusion and field diffraction. Namely, we solve the linear equations

$$\frac{\partial}{\partial t} N = \mu D \frac{\partial^2}{\partial x^2} N, \qquad \left(\frac{\partial}{\partial t} \pm \frac{\partial}{\partial z}\right) E^{\pm} = -\frac{i}{2}\frac{\partial^2}{\partial x^2} E^{\pm}$$

within the time (and space) interval of length h, whereas the initial conditions are given by the previously obtained estimates $\widetilde{N}$ and $\widetilde{E}^{\pm}$. To integrate these equations we use lateral discretizations of the functions N and $E^{\pm}$, approximate their second lateral derivatives by (8) and solve the resulting systems of the differential equations in the (lateral) Fourier domain:

$$\widehat{N}_\ell(z, t+h) = e^{-\mu D \frac{\pi^2 \ell^2}{X^2} h} \widehat{N}_\ell(z,t), \qquad \widehat{E}^{\pm}_\ell(z \pm h, t+h) = e^{i\frac{\pi^2\ell^2}{2X^2} h} \widehat{E}^{\pm}_\ell(z,t).$$

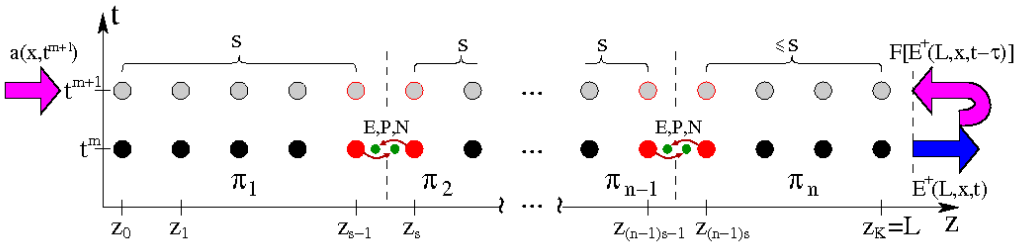

Figure 2: Scheme of the computational grid (z and t coordinates only). Vertical dashed lines: splitting of the grid Q_h^X to smaller sub-grids $Q_h^{X,l}$. Full and grey shaded bullets: the actual (already computed) and the next time layers, respectively. Arrows: data streams which should be read or recorded by different processes π_l before the next time iteration. Green dots: ghost points of the sub-grid containing an information received from the corresponding border point (red bullets) of the adjacent sub-grid.

The inverse discrete Fourier transform (6) and the discretization of the functions N and $E^{\pm}$ along the longitudinal z direction give us the following equations, which completes the description of our numerical scheme:

$$\begin{aligned} N^{m+1}_{k,j} &= \frac{1}{J}\sum_{\ell=-J/2}^{J/2-1}\left[e^{-\mu D\frac{\pi^2\ell^2}{X^2}h}\sum_{s=-J/2}^{J/2-1}\widetilde{N}^{m+1}_{k,s}e^{-i\frac{2\pi\ell s}{J}}\right]e^{i\frac{2\pi\ell j}{J}}, \\ E^{\pm,m+1}_{k,j} &= \frac{1}{J}\sum_{\ell=-J/2}^{J/2-1}\left[e^{i\frac{\pi^2\ell^2}{2X^2}h}\sum_{s=-J/2}^{J/2-1}\widetilde{E}^{\pm,m+1}_{k,s}e^{-i\frac{2\pi\ell s}{J}}\right]e^{i\frac{2\pi\ell j}{J}}, \\ &k = 0,\dots,K, \qquad j = 1,\dots,M. \end{aligned} \tag{11}$$

3.2 Parallelization

Our problem (1)-(5) and the numerical scheme (9)-(11) are well suited for the execution on parallel compute clusters using distributed memory techniques. To distribute the computational work among different processes $\pi_l|_{l=1}^n$ we decompose the computational grid Q_h^X along the longitudinal z- direction into n non-overlapping sub-grids $Q_h^{X,l}$. The first $n-1$ sub-grids $Q_h^{X,l}$ have s longitudinal grid points z_k each, whereas the number of z_k in the last sub-grid is smaller or equal to s. In such a manner, any process π_l operates on the sub-grid

$$\begin{aligned} &Q_h^{X,l} = \omega_{h,z}^l \times \omega_{h,x} \times \omega_{h,t}, \qquad \omega_{h,z}^l = \omega_{h,z} \cap \left[(l-1)sh, \min\{(ls-1)h, L\}\right], \\ &s = \text{ceil}\left((K+1)/n\right), \qquad l = 1,\dots,n. \end{aligned}$$

A schematic representation of the full computational grid and its splitting to smaller sub-grids is given in Fig. 2).

Before computing the grid functions at the next time layer (grey shaded bullets in Fig. 2) each process π_l should exchange the current time layer values of $E^{\pm}$, $P^{\pm}$ and N at the boundaries of the sub-grid $Q_h^{X,l}$ (red bullets in the same figure) with the adjacent processes π_{l-1} and π_{l+1}. This information is recorded to the specially created ghost grid points (green dots) at the adjacent side of the sub-grids $Q_h^{X,l-1}$ and $Q_h^{X,l+1}$. The left and right ghost points of the sub-grid $Q_h^{X,l}$ in the consequent computations of the process π_l are treated like usual grid points $(z_{(l-1)s-1}, x_j, t^m)$ and (z_{ls}, x_j, t^m) which are not directly accessible by π_l.

The processes π_1 and π_n operating on the end sub-grids $Q_h^{X,1}$ and $Q_h^{X,n}$ have no left or right adjacent sub-grid. The required sub-grid boundary information in these cases is given by the longitudinal boundary conditions (4) including optional optical injection and optical feedback functions $a(x,t)$ and $F[E^+(L,x,t-\tau)]$ (violet in-pointing arrows in the same figure). The scalability analysis of the proposed parallel algorithm can be done as in [5]. It proves that the algorithm scales linearly with respect to the number of processors used to solve the given problem.

In additional to the solution of the scheme (9)-(11) on the sub-grid $Q_h^{X,n}$, the last process π_n records the emitted field $E^+(L,x,t)$ and calculates distributions of the optical feedback (if considered). Thus, the fact that $Q_h^{X,n}$ has, possibly, less grid points then the other sub-grids (size of $\omega_{h,z}^n$ can be smaller than s) could be advantageous seeking to speed up the simulations.

The numerical scheme (9)-(11) and the parallel algorithm were implemented and executed on a 48 node HP Blade server using the HPMPI library. The nodes are interconnected via Infiniband 4xDDR (20 Gbit/s).

4 Simulations of BAS devices

Mathematical modeling and fast numerical simulations are a powerful method used in optimization of the existing BAS devices or in creation of the novel design concepts for different real world applications. Below in this section we simulate two theoretically proposed BAS devices (shown also in Fig. 1(b) and (c)) showing an improved quality of the emitted beam.

4.1 Stabilization of a BAS laser by a dual off-axis optical injection

In our theoretical papers [12, 13] a new control method of BAS lasers was proposed, which, as we believe, should suppress all but one optical mode, i.e., should stabilize the emitted beam. This control is achieved by a pair of coherent optical plane waves injected into the BAS laser at the adjacent angles to the laser axis (Fig. 1(b)). Mathematically, this optical injection is described by the function

$$a(x,t) = a_0 e^{i(\omega t + 2\pi x\alpha/\lambda_0 - \pi/2)} + a_0 e^{i(\omega t - 2\pi x\alpha/\lambda_0 + \pi/2)} = 2a_0 e^{i\omega t} \sin(\alpha k_0 x)$$

entering boundary conditions (4). The parameters $\pm\alpha$, λ_0 and ω in the expression above denote the free space angles of the injected beams (see Fig. 1(d)), the central wavelength of the emitted field, and the frequency detuning of the optical injection from the central frequency $\frac{2\pi c}{\lambda_0}$ (c: speed of light in vacuum). The factor $|a_0|^2$ is proportional to the intensity of the optical field injected into the laser.

We have performed a series of simulations for the fixed detuning ($\omega = 0$ in this example) and increased intensity of the optical injection (i.e., parameter $|a_0|^2$). The observed laser dynamics (optical spectra, far-fields, field intensities) for different injection intensities is summarized in

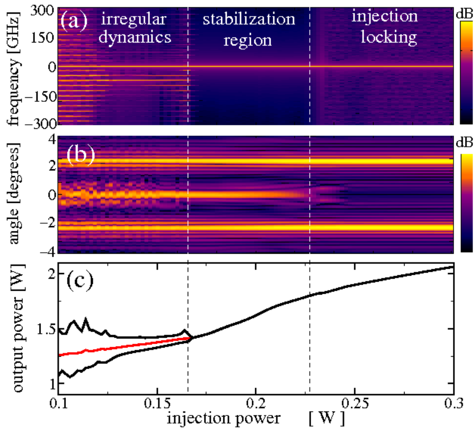

Figure 3: Stabilization of the BAS laser by the optical injection. (a): mapping of the optical spectra, (b): mapping of the far-fields computed at some time instant, and (c): maximal, minimal and mean power of the emitted field for the increased injection power and fixed $\omega = 0$.

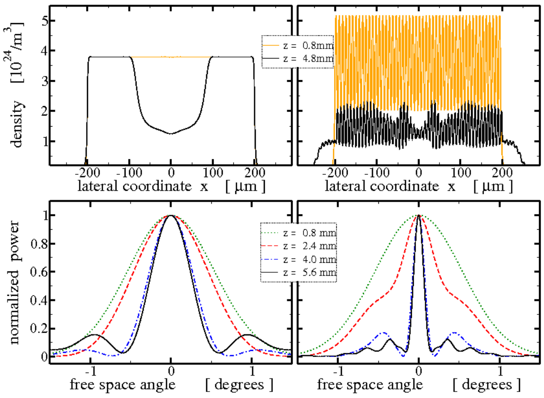

Figure 4: Amplification of the optical beam in the equally biased conventional (left) and the PM EE BAS amplifiers with $(d_x, d_z) = (8, 400)\,\mu$m, and $\mathcal{Q} = 1.02$ (right). First and second rows show lateral distributions of the carrier density and central part of the far-fields computed for selected longitudinal positions z.

Fig. 3. Here one can distinguish three qualitatively different regimes, separated by thin vertical lines in Fig. 3. Once the injection intensity is too small, the spatial-temporal dynamics of the system is similar to that one of the free-running BAS laser. This can be recognized by multiple peaks of the optical spectrum (panel (a)), by scattered far-field instants (panel (b)), as well as by a non-stationary output field (differing minimal and maximal intensities in panel (c)). For moderate and large injected field intensities the laser operates at a continuous wave regime (a single spectral line in panel (a) and coinciding minimal and maximal powers in panel (c)). An inspection of the far-fields at these injections, however, allows us to distinguish two different regimes. Namely, for moderate injections we have a stationary state which has a well pronounced central angular component (a stabilized mode of the laser), whereas for larger injections only the angular components corresponding to the injected beam angles α are present. In this regime our BAS laser is operating like an amplifier for the injected beams, but does not generate light by itself.

4.2 BAS amplifiers with periodically modulated electrical contacts

An elegant way to improve the lateral beam profile in EE BAS amplifiers was suggested in the recent theoretical work [14]. It was shown, that a periodic modulation of the gain and refractive index in both longitudinal and lateral directions (see Fig. 1(c)) can lead to a significant compression of the far-fields, what is desirable in the real world applications.

A crucial condition for the desired beam shaping is a proper choice of the lateral and longitudinal modulation periods d_x and d_z, which should satisfy the relation

$$\mathcal{Q} = \frac{2d_x^2 n_b}{\lambda_0 d_z} \approx 1,$$

where n_b is the background refractive index in the semiconductor device (typically about $3 \div 3.5$). The mathematical model used in [14], however, was oversimplified: it was neglecting a strong nonlinear interaction of carriers and optical fields in high-power devices, i.e., was only suitable for simulations of very small fields (and polarizations) which have no impact to the carrier distribution (see the carrier rate equation in Eq. (1)).

In the present work we have performed simulations of the standard BAS amplifier (left panels of Fig. 4) and of the BAS amplifier with the PM electrical contact (right panels of the same figure) operating in moderate and high power regimes. In these regimes the carrier distribution is strongly depleted, causing also lateral irregularities in the carrier (i.e., gain and refractive index) modulation amplitudes: see the black curves in the second row panels of Fig. 4, representing the carrier densities at $z = 4.8$ mm. The simulations have shown, that the desired beam shaping in the PM BAS amplifiers can be also obtained using our more realistic modeling approach. It can be seen when comparing the far-fields of the simple (left) and PM amplifiers (right) at the lower row panels of this figure. It is noteworthy, that even though a part of the field amplified in the PM device is radiated at the side band components at $\approx \pm 7.2°$, the intensity of the remaining central angle field still can be higher than that one of the field amplified in the conventional BAS device (compare the upper row panels).

Acknowledgments.

The authors would like to thank Mark Lichtner for implementation of the numerical schemes on the parallel compute cluster.

References

[1] Wenzel, H.: Basic aspects of high-power semiconductor laser simulation. to appear in IEEE J. of Select. Topics in Quantum Electron. 19, (2013)

[2] Bandelow, U., et. al.: Impact of gain dispersion on the spatio-temporal dynamics of multisection lasers. IEEE J Quantum Electron. 37, 183–188 (2001)

[3] Spreemann, M., et. al.: Measurement and simulation of distributed-feedback tapered Master-Oscillators Power-Amplifiers. IEEE J. of Quantum Electron. 45, 609–616 (2009)

[4] Lichtner, M., Radziunas, M., Recke, L.: Well posedness, smooth dependence and center manifold reduction for a semilinear hyperbolic system from laser dynamics. Math. Meth. Appl. Sci. 30, 931–960 (2007)

[5] Čiegis, R., Radziunas, M., Lichtner, M.: Numerical algorithms for simulation of multisection lasers by using traveling wave model. Math. Model. Anal. 13, 327–348 (2008)

[6] Laukaityte, I., et. al.: Parallel numerical algorithm for the traveling wave model. In: R. Ciegis, R., Henty, D., Kagstrom B., Zilinskas, J. (eds.) Parallel Scientific Computing and Optimization vol. 27, pp. 237–251. Springer (2009)

[7] Čiegis, R., Radziunas, M.: Effective numerical integration of traveling wave model for edge-emitting broad-area semiconductor lasers and amplifiers. Math. Model. Anal. 15, 409–430 (2010)

[8] Radziunas, M., et. al.: Mode transitions in distributed-feedback tapered master-oscillator power-amplifier. Opt. and Quantum Electron. 40, 1103–1109 (2008)

[9] Tronciu, V.Z., et. al.: Improving the stability of distributed-feedback tapered master-oscillator power-amplifiers. Opt. and Quantum Electron. 41, 531–537 (2009)

[10] Jechow, A., et. al.: Stripe-array diode-laser in an off-axis external cavity: Theory and experiment. Optics Express 17, 19599–19604 (2009)

[11] Tronciu, V.Z., et. al.: Amplifications of picosecond laser pulses in tapered semiconductor amplifiers: Numerical simulations versus experiments. Opt. Communications 285, 2897–2904 (2012)

[12] Radziunas, M., Staliunas, K.: Spatial rocking in broad area semiconductor lasers. Europhysics Letters 95, 14002 (2011)

[13] Radziunas, M., Staliunas, K.: Spatial ”rocking” for improving the spatial quality of the beam of broad area semiconductor lasers. In: SPIE proc. 8432, 84320Q (2012)

[14] Herrero, R., et. al.: Beam shaping in spatially modulated broad area semiconductor amplifiers. Optics Letters 37, 5253–5255 (2012)